STUDY ON PREHEATING AND TEMPERATURE MAINTENANCE PERFORMANCE OF AN INTEGRATED THERMAL MANAGEMENT SYSTEM DURING CHARGING

Yong Liu[1,2*], Mohan Hu[1], Yige Chen[1], Xuehong Wu[1,2], Shang Mao[1,2], and Yanling Wang[1,2]

[*1]School of Energy and Power Engineering, Zhengzhou University of Light Industry, Zhengzhou, Henan 450000, China

[2]International Joint Laboratory of Energy Efficiency Conversion and Utilization of Henan Province, Zhengzhou 450000, China

[*] Corresponding author; E-mail: yliu@zzuli.edu.cn

In low-temperature environments, incomplete internal reactions during charging and discharging can degrade battery capacity and reduce efficiency. To address this, the study explores the use of electric heating films for preheating and thermal insulation in a battery thermal management system, integrated with phase-change liquid cooling for temperature control and thermal runaway suppression. First, the impact of heat flux density and heating surface layouts on heating efficiency was analyzed with the liquid cooling system deactivated. The results show that heat flux density significantly affects temperature differences during preheating. Simultaneously heating the minor side and bottom surfaces improves preheating efficiency, and heating both the battery and battery thermal management system together reduces the temperature difference. With a heating power of 2000 [Wm^{-2}], the battery reached 25 °C from an initial temperature of 0 °C in 1769 seconds. In the 1 C charging and thermal maintenance phase, activating the liquid cooling system and setting the heating power to 200 [Wm^{-2}] kept the minimum battery temperature around 27 °C, with a temperature difference of 2.6 °C.

Key words: *lithium-ion batteries, phase change material structure, porous metal foam, liquid cooling tube, preheating*

1. Introduction

When lithium-ion batteries (LIBs) are charged in low-temperature environments, issues like reduced efficiency, capacity degradation, and accelerated fading arise [1]. These problems are caused by two main factors. First, low temperatures increase the electrolyte's viscosity, slowing electrochemical reactions, reducing capacity, and increasing internal resistance. Second, charging in cold conditions promotes lithium dendrite formation, which obstructs ion transport and reduces charging efficiency [2,3]. To mitigate these effects, three common methods include external alternating current (AC) electric field heating for rapid temperature rise, in-situ heating through internal self-heating via pulsed discharge, and external preheating with heat sources before charging to elevate battery temperature. While self-heating offers faster heating with less battery aging impact, it poses higher safety risks. External methods, though simpler, have longer heating times and higher energy losses [1]. AC heating has been

widely studied, but it can damage the battery structure and requires extra power supply, reducing lifespan. To overcome these, Cui *et al*. [4] proposed high-frequency AC heating using a bidirectional boost converter, achieving 4.65 [°Cmin^{-1}] at 800 Hz. Ghassemi *et al*. [5] tested high-amplitude AC harmonics and charge-discharge cycles, finding minimal cycle life impact if voltage oscillations remained below a threshold. In pulsed discharge self-heating, Tang *et al*. [6] developed an electro-thermal aging model to explore how pulsed preheating improves environmental adaptability and lifespan. Zhuang *et al*. [7] studied the impact of low-frequency, high-amplitude pulses on battery degradation, revealing the aging mechanisms through relaxation time distribution. While these internal methods have drawbacks, such as not completing preheating before activation, they enhance practical applications compared to external methods, which preheat batteries to optimal temperatures before use. Research on external preheating approaches includes air cooling, heat pipes, liquid cooling, and phase change materials (PCM) within the battery thermal management system (BTMS) [8]. Xu *et al*. [9] proposed an integrated heating and cooling system using a heat sink plate, showing a 6.98 [°Cmin^{-1}] heating rate at -20 °C with 69.8% efficiency at a 3 C discharge rate. Bao *et al*. [10] studied single-phase immersion preheating and found it improved low-temperature battery performance. An *et al*. [11] combined liquid cooling and thermoelectric cooling, proposing an optimal segmented preheating strategy for improved performance. Zhong *et al*. [12] designed a preheating system using a topology-optimized liquid cooling plate, achieving a 24.8% heating rate improvement. In heat pipe research, Ren *et al*. [13] developed a BTMS based on a U-shaped micro heat pipe array, achieving preheating from -20 °C to 0 °C in 26 minutes with 32 W of heating. Liang *et al*. [14] achieved integrated preheating and cooling with a bent-flat-plate micro heat pipe array, reaching a 1 [°Cmin^{-1}] temperature rise rate at -20 °C, with minimal temperature difference. In phase change cooling, Chen *et al*. [15] combined PCM with heating plates, exploring the effects of structure and spacing. An *et al*. [16] integrated PCM with honeycomb liquid cooling tubes, enabling rapid heating in about 6 minutes. Zhang *et al*. [17] tested heating film placement, finding that bottom heating resulted in poorer uniformity compared to side heating. E *et al*. [18] combined heating films and PCM for high-capacity NMC lithium-ion batteries, achieving superior preheating performance.

Current research primarily focuses on battery preheating, with less attention on maintaining temperature stability during charging. Self-heating from internal chemical reactions and current flow affects battery temperature during charging. While thermal management during normal temperatures and preheating has been studied, the role of electric heating films in integrated BTMS and their impact on preheating performance is often overlooked. This study builds on a previous integrated phase-change liquid-cooling system for temperature control and thermal runaway suppression, exploring the optimization of the preheating system using electric heating films [19]. It aims to select heating film types and optimize surface layouts to improve heating rates and reduce internal temperature differences. In low temperatures, when liquid cooling cannot provide 25 °C coolant, the system switches to electric heating. The study focuses on activating liquid cooling and adjusting heat flux density to maintain stable battery temperatures between 25 °C and 45 °C during 1 C charging, minimizing temperature differences.

2. Physical problem description and numerical model

2.1. Physical model of the battery thermal management system

Figure 1 (a) presents the BTMS geometric model, combining PCM and liquid cooling. It has a

sandwich structure with microchannel liquid cooling tubes (LCT) embedded between high and low-conductivity PCM layers. The layered structure PCM includes high thermal conductivity phase change material (HPCM) and low thermal conductivity phase change material (LPCM), where HPCM is the composite PCM composed of PCM n-nonadecane and porous metal foam copper, while LPCM is the pure PCM n-nonadecane. The LCT uses a single-tube dual-channel counter-flow design, filled with copper foam (porosity 0.86) to enhance heat transfer. A 5 mm high-conductivity PCM layer surrounds the battery, while the remaining area has a 2 mm low-conductivity PCM layer. The specific physical properties are shown in Tab. 1. The six heating schemes are shown in Fig. 1 (b). Case 1: heating the battery's minor side; Case 2: heating the battery's bottom; Case 3: heating the battery's minor side and bottom; Case 4: heating both the minor side of the battery and BTMS; Case 5: heating both the bottom of the battery and BTMS; Case 6: heating both the minor side and bottom of the battery and BTMS.

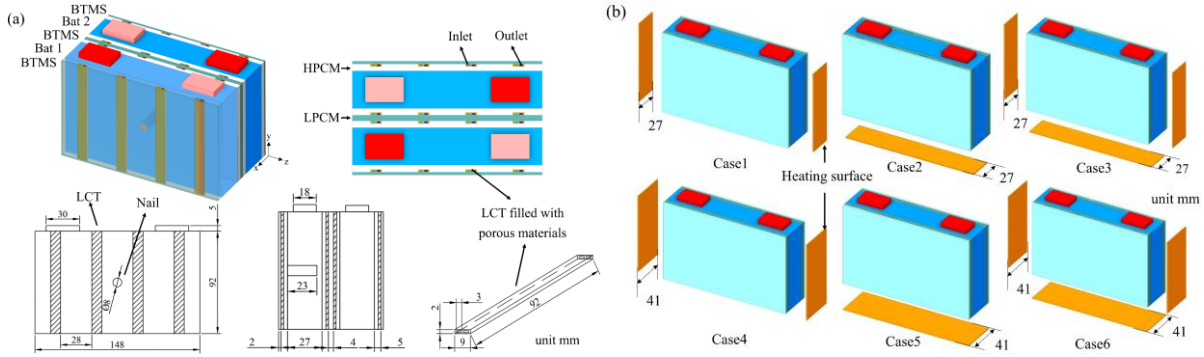

Figure 1. Phase change liquid cooling integrated BTMS and heating surface selection, (a) Phase change liquid cooling integrated BTMS, (b) Heating surface selection

Table 1. Material properties

Parameter	LIB [21]	Copper [22]	PCM [23]	Water [24]
Density ρ (kgm^{-3})	2312	7850	782	998.2
Specific heat capacity C_p ($Jkg^{-1}k^{-1}$)	1068	475	1910	4182
Heat conductivity λ ($Wm^{-1}k^{-1}$)	λ_x=1 λ_y=λ_z=26.6	44.5	0.21	0.6
Capacity C (Ah)	50	/	/	/
Working voltage U (V)	3.7	/	/	/
Latent heat γ ($Jkg^{-1}K^{-1}$)	/	/	222000	/
Melting temperature T(°C)	/	/	32	/

2.2. Model assumptions

The following assumptions simplify the BTMS mathematical model：

(1) The battery's specific heat capacity, thermal conductivity, and internal resistance are constant during charging and discharging. The entropy change of internal reactions is temperature-independent, and the heating rate is based on an initial temperature of 25 °C.

(2) Local thermal equilibrium is satisfied between the PCM and the porous metal skeleton.

(3) The porous medium is isotropic, and the thermophysical properties of the PCM, coolant, and porous metal are constant. Fluid flow in the porous metal is incompressible, with no viscous dissipation.

(4) Thermal resistance due to contact and any relative motion between batteries, and between batteries and the PCM, are neglected.

2.2.1 Mathematical model of heat generation in LIBs during charging and discharging

The three-dimensional thermal model of the battery module is given by Eq. (1). The Bernardi model [25], a coupled electro-thermal model, is used to calculate the volumetric heat generation rate based on battery parameters. It assumes that battery heat is generated by reversible electrochemical reactions and Joule heating. The expression for the volumetric heat generation rate, derived from previous studies, is given by Eq. (2). Where, q_a represents the volumetric heat generation rate of the battery during charging and discharging. According to the predicted heat generation formula, the volumetric heat generated per unit volume under different discharge rates are 11246.4 [Wm^{-3}] at 1 C, 24325.27 [Wm^{-3}] at 1.5 C, 24325.27 [Wm^{-3}] at 2 C, 93384.56 [Wm^{-3}] at 3 C.

$$\rho_b C_{p,b}\frac{\partial T}{\partial \tau} = Q + \frac{\partial}{\partial x}(\lambda_x \frac{\partial T}{\partial x}) + \frac{\partial}{\partial y}(\lambda_y \frac{\partial T}{\partial y}) + \frac{\partial}{\partial z}(\lambda_z \frac{\partial T}{\partial z}) \tag{1}$$

$$q_a = \frac{Q_a}{V} = \frac{0.00137I^2 - 0.044I}{148\times150\times27\times10^9} = 3.98I^2 + 2.611I \tag{2}$$

2.2.2 Numerical model of phase change material cooling in porous metals

The continuity, momentum, and energy equations for the phase change material within the porous metal are given by Eq. (3-5) [26, 27].

$$\frac{\partial \rho_{PCM}}{\partial t} + \nabla\cdot(\rho_{PCM}\vec{V}) = 0 \tag{3}$$

$$\rho_{PCM}\frac{\partial v_x}{\partial t} + \rho_{PCM}(\nabla\cdot\vec{V})v_x = \mu_{PCM}\nabla^2 v_x - \frac{\partial P}{\partial x} + f_1\frac{(1-f)^2}{f^3+\delta}v_x - \frac{\mu}{K}v_x - \frac{\rho_{PCM}C_i}{\sqrt{K}}|v_x|v_x \tag{4-1}$$

$$\rho_{PCM}\frac{\partial v_y}{\partial t} + \rho_{PCM}(\nabla\cdot\vec{V})v_y = \mu_{PCM}\nabla^2 v_y - \frac{\partial P}{\partial y} + f_1\frac{(1-f)^2}{f^3+\delta}v_y - \frac{\mu}{K}v_y - \frac{\rho_{PCM}C_i}{\sqrt{K}}|v_y|v_y + \rho_{PCM}g\beta\phi(T-T_{ref}) \tag{4-2}$$

$$\rho_{PCM}\frac{\partial v_z}{\partial t} + \rho_{PCM}(\nabla\cdot\vec{V})v_z = \mu_{PCM}\nabla^2 v_z - \frac{\partial P}{\partial r} + f_1\frac{(1-f)^2}{f^3+\delta}v_z - \frac{\mu}{K}v_z - \frac{\rho_{PCM}C_i}{\sqrt{K}}|v_z|v_z \tag{4-3}$$

$$\frac{\partial\left[(1-\phi)(\rho_s h_s) + \phi(\rho_{PCM}h_{PCM})\right]}{\partial t} + \rho_{PCM}(\vec{V}\cdot\nabla\cdot h_{PCM}) = \lambda\nabla^2 T \tag{5}$$

The enthalpy of the PCM and the porous metal can be obtained from Eq. (6-8).

$$f_l = \begin{cases} 0 & T < T_m \\ 1 & T > T_m \end{cases} \tag{6}$$

$$h_{PCM} = h_{ref} + \int_{T_{ref}}^{T} C_{p,PCM}dT + f_l\gamma \tag{7}$$

$$h_s = h_{ref} + \int_{T_{ref}}^{T} C_{p,s}dT \tag{8}$$

2.2.3 Numerical model of coolant heat transfer in porous metals

The continuity, momentum, and energy equations for the coolant are given by Eq. (9-11) [27].

$$\frac{\partial \rho_w}{\partial t} + \nabla\cdot(\rho_w\vec{V}) = 0 \tag{9}$$

$$\rho_w \frac{\partial v_x}{\partial t} + \rho_w (\nabla \cdot \vec{V}) v_x = -\frac{\partial P}{\partial x} + \mu_w \nabla^2 v_x - \frac{\mu_w}{K} v_x - \frac{\rho_{PCM} C_i}{\sqrt{K}} |v_x| v_x \tag{10-1}$$

$$\rho_w \frac{\partial v_y}{\partial t} + \rho_w (\nabla \cdot \vec{V}) v_y = -\frac{\partial P}{\partial y} + \mu_w \nabla^2 v_y - \frac{\mu_w}{K} v_y - \frac{\rho_{PCM} C_i}{\sqrt{K}} |v_y| v_y + \rho_w g \beta \phi (T - T_{ref}) \tag{10-2}$$

$$\rho_w \frac{\partial v_z}{\partial t} + \rho_w (\nabla \cdot \vec{V}) v_z = -\frac{\partial P}{\partial z} + \mu_w \nabla^2 v_z - \frac{\mu_w}{K} v_z - \frac{\rho_{PCM} C_i}{\sqrt{K}} |v_z| v_z \tag{10-3}$$

$$\frac{\partial [(1-\phi)(\rho_s h_s) + \phi(\rho_w h_w)]}{\partial t} + \rho_w (\vec{V} \cdot \nabla \cdot h_w) = \lambda \nabla^2 T \tag{11}$$

2.2.4 Boundary conditions

The heat transfer between the battery, PCM, and the surrounding environment is natural convection, with the convective heat transfer equation given by Eq. (12). the natural convection coefficient h is taken as 5 [$Wm^{-2}°C^{-1}$].

$$Q_h = hS(T_{wall} - T_{air}) \tag{12}$$

2.2.5 Validation of the BTMS numerical model

To validate the proposed BTMS numerical model, simulations were performed for both the battery heat generation during charging and discharging and the phase-change liquid-cooling coupled heat transfer model. The results were consistent with experimental data from previous studies [19]. The battery heat generation model was based on Xu *et al*. [21], with average surface temperatures monitored under various discharge currents, with a maximum relative error of less than 5%. The liquid-cooling model was based on Zhang *et al*. [28], also monitoring the average surface temperature, with a maximum relative error of less than 3%. Both simulations showed good agreement with experimental data, confirming the model's reliability. Mesh and time step independence were verified through simulations focusing on the maximum battery temperature and liquid fraction of PCM at the end of the 3C discharge process. Mesh independence was confirmed with over 455951 grids, and time step independence was achieved with steps smaller than 1 second. Therefore, the final simulation used 455951 mesh elements and a 1 second time step for all calculations.

3. Results and discussion

3.1 Effects of different heat flux densities and heating surface configurations on battery preheating

Heating films, powered by a constant-voltage supply, have a heat flux density that depends on material resistance and thickness, independent of the heating area [17]. This study investigates the impact of heat flux and heating surface layout on the preheating performance of prismatic battery cells using a coupled model of the battery and BTMS. The study consists of two parts. The first part analyzes the effects of varying heat flux density (1000-5000 [Wm^{-2}]) on the battery's temperature rise rate and uniformity to guide heating film selection. The second part compares different heating surface layouts under identical power conditions to identify the optimal configuration for heating efficiency and uniformity. The goal is to heat the battery to 25 °C within 3600 seconds. Given that both the initial system and ambient temperatures are 0 °C, and the liquid cooling system cannot provide 25 °C coolant

quickly, the cooling system is deactivated to simulate real operating conditions.

3.1.1 Effect of different heat flux densities on battery preheating

Heating rate and temperature uniformity are key metrics for evaluating battery heating performance. Figure 2 (a-f) shows that as heat flux density increases from 1000 [Wm^{-2}] to 5000 [Wm^{-2}], the minimum battery temperature rises faster, indicating that higher heat flux improves heating speed. For example, Case 6 reaches the desired temperature in 786 seconds at 5000 [Wm^{-2}], while at 1000 [Wm^{-2}], it only reaches 20.36 °C after 3600 seconds. Moreover, schemes with larger heating areas achieve faster heating rates due to higher total heating power, as seen in Case 2 and Case 6.

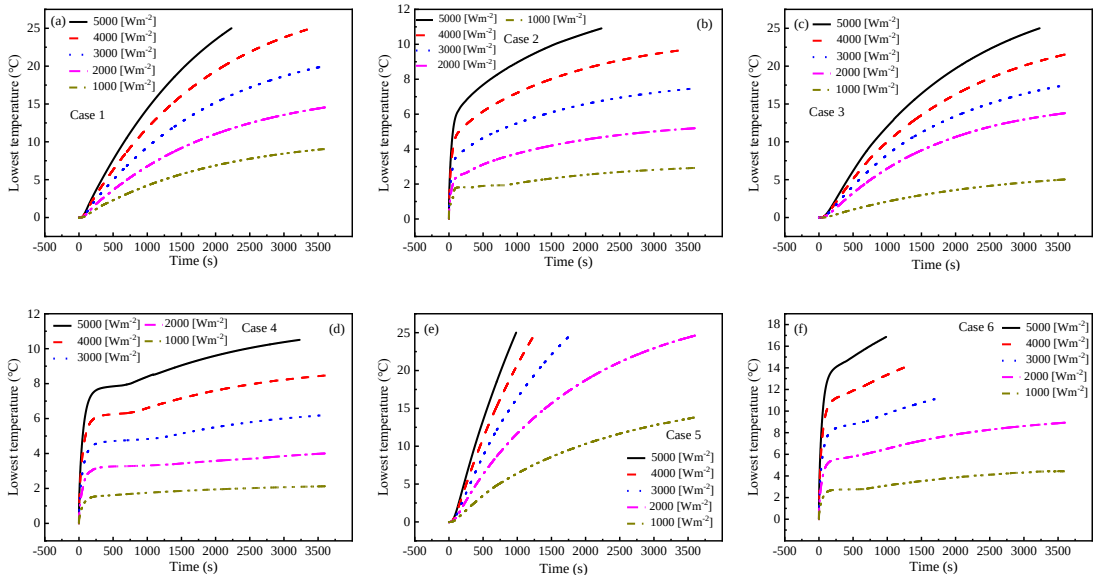

Figure 2 Variation of the minimum battery temperature with time for different heating schemes

Figure 3 (a-f) shows a rapid increase in temperature difference during the preheating stage, followed by either a slight decrease or gradual rise. In Case 6 at 5000 [Wm^{-2}], the temperature difference peaks at 14 °C at 170 seconds and slowly rises to 15.01 °C by 625 seconds. At 1000 [Wm^{-2}], the temperature difference fluctuates. The initial rise occurs because the heating rate exceeds the battery material's thermal diffusion capacity. comparing Case 1 with Case 2 and Case 4 with Case 5, the trends are similar. This indicates that the temperature difference during preheating is influenced not only by the heating surface arrangement, but also significantly by the magnitude of the heat flux density. Thus, while increasing the heat flux density helps accelerate the heating speed, it also leads to a larger temperature difference. Analysis shows that with the same heat flux density, heating rates follow Case 4 > Case 1, Case 5 > Case 2, and Case 6 > Case 3, while the temperature difference trends oppositely. Higher power improves efficiency. The copper foam in the BTMS acts as a thermal bridge, reducing temperature non-uniformity by transferring heat from the battery surface to its interior. Heating both the battery and BTMS together improves both efficiency and uniformity.

In summary, increasing heat flux density accelerates heating but also increases temperature difference. A balance between heat flux, heating rate, and temperature uniformity is necessary. None of the schemes could control the temperature difference within 5 °C, but Case 6 (2000 [Wm^{-2}]) and Case 4 (3000 [Wm^{-2}]) kept it below 8 °C. Case 6, however, shows a clear advantage in heating efficiency, completing heating in 1769 seconds, which is a reduction of 31.49% compared to Case 4. Therefore,

Case 6 (2000 [Wm^{-2}]) is chosen as the baseline scheme for further research.

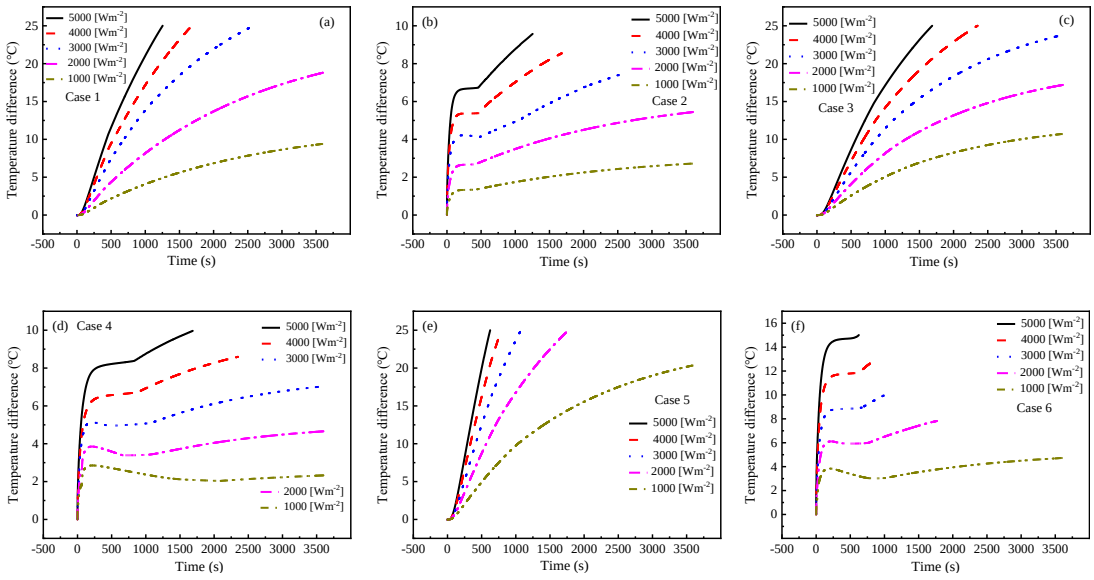

Figure 3 Temperature difference with time for different heating schemes

3.1.2 Effects of different heating surface configurations on battery preheating

Under constant total heating power (with Case 6 at 2000 [Wm^{-2}] as the baseline), the heating surface layout greatly impacts efficiency and temperature difference. As shown in Fig. 4 (a), Case 6 completes heating in 1769 seconds with a temperature difference of 7.82 °C, showing the best performance. Heating efficiency ranks: Case 6 > Case 3 > Case 2 > Case 4 > Case 1 > Case 5, with Cases 1, 2, 4, and 5 showing similar efficiency. This ranking depends on heat flux density and heating surface layout. For example, Case 2's higher flux density improves efficiency but increases the temperature difference compared to Case 1. Case 5 is less efficient than Case 4 due to higher heat absorption by the BTMS.

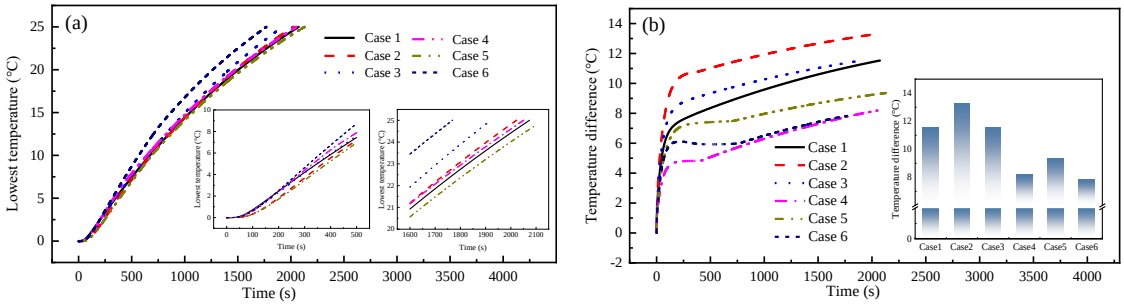

Figure 4. Effect of different heating surface configurations on the minimum temperature and temperature difference, (a) Minimum temperature, (b) Temperature difference

Fig. 4 (b) ranks the temperature differences: Case 6 < Case 4 < Case 5 < Case 1 < Case 3 < Case 2. Heating both the battery and BTMS simultaneously is more effective at controlling temperature differences, as the PCM in the BTMS evenly distributes heat, reducing local overheating. Case 6, with heating on both the sides and bottom, the temperature difference is reduced by 32.3% compared to Case 3 due to its lower heat flux density. In conclusion, under equal power, using lower heat flux density while heating both the side and bottom of the battery and BTMS yields superior preheating performance.

3.2 Study on thermal maintenance during 1C charging after preheating

Building on the preheating scheme for the side and bottom surfaces of the battery and BTMS (with 2000 [Wm^{-2}] heating power) from Section 3.1, this section further explores the thermal maintenance strategy during charging after preheating for Case 6. An incremental optimization method, starting from 0 and increasing heating power by 100 [Wm^{-2}] steps, is used to determine the optimal dynamic heating configuration. The study examines two conditions: Condition 1, where 1 C charging starts after the battery reaches 25 °C with deactivated liquid cooling; and Condition 2, where 1 C charging begins after the battery reaches 25 °C with liquid cooling enabled, supplying 25 °C coolant at 0.006m/s. This analysis focuses on the required heating power for temperature maintenance after liquid cooling is activated. By comparing the thermal management performance in both conditions, including the minimum battery temperature and temperature difference, the optimal heating power control strategy is determined for achieving the best thermal management during charging. The specific scheme is shown in Fig. 5.

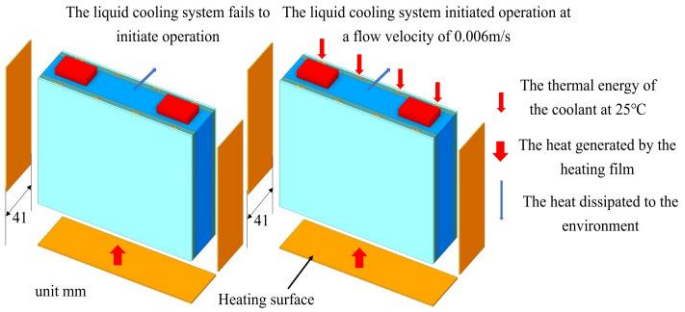

Figure 5. Schematic of the liquid cooling system deactivation or activation after battery preheating

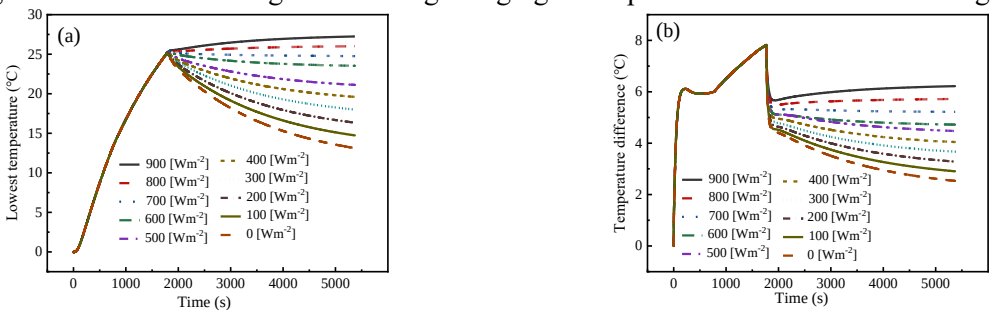

(a) Minimum temperature **(b) Temperature difference**

Figure 6. Variation of the minimum battery temperature and temperature difference with time after battery preheating with liquid cooling deactivated (Case 6 scheme)

Figure 6 shows the variation in minimum battery temperature and temperature difference over time for Case 6 (heating both the minor side and bottom of the battery and BTMS) after preheating and deactivating the liquid cooling system. After preheating at 2000 [Wm^{-2}], both the minimum temperature and temperature difference exhibit clear inflection points. Below 700 [Wm^{-2}] heating power, the minimum temperature continues to decrease, dropping to 24.76 °C at the end of 1 C discharge at 700 [Wm^{-2}]. Above 800 [Wm^{-2}], the minimum temperature increases slowly, reaching 26.01 °C at the end of discharge at 800 [Wm^{-2}] (Fig. 6 (a)). Regarding temperature difference (Fig. 6 (b)), it initially drops rapidly and then follows different trends. Above 800 [Wm^{-2}], the temperature difference gradually increases, while it decreases below 800 [Wm^{-2}]. Thus, with the cooling system deactivated, a heating power above 800 [Wm^{-2}] is needed to maintain a minimum temperature above 25 °C. The temperature difference stabilizes around 5.8 °C, slightly exceeding the ideal range.

Figure 7 shows the variation in minimum battery temperature and temperature difference over

time for Case 6 (heating both the minor side and bottom of the battery and BTMS) after activating the liquid cooling system. Similar to the deactivated cooling case, both the minimum temperature and temperature difference show an inflection point after the 2000 [Wm^{-2}] preheating stage. However, with cooling active, the minimum temperature briefly increases due to heat release from the PCM and the flowing liquid in the cooling tube, which transfers heat to the battery. With liquid cooling on (Fig. 7 (a)), the battery temperature stays above 25 °C, reaching 25.61 °C by the end of the 1 C charge, even with 0 [Wm^{-2}] heating. To maintain stability during charging, 200 [Wm^{-2}] heating is needed. Under this condition, the temperature distribution of the battery shows that the surface temperature of the battery finally reached 27.07 °C. For the temperature difference (Fig. 7 (b)), it initially drops quickly, then either decreases slowly or increases. The critical threshold is 200 [Wm^{-2}]: above this, the temperature difference rises slowly; below this, it continues to decrease. To maintain a stable minimum temperature above 25 °C and a favorable temperature difference, 200 [Wm^{-2}] is recommended. Under this condition, the minimum temperature fluctuates by only 0.23 °C over 3000 seconds. Accordingly, the temperature distribution shows that the surface temperature difference of the battery remains around 2.57 °C with a fluctuation of just 0.09 °C, both within the desired range.

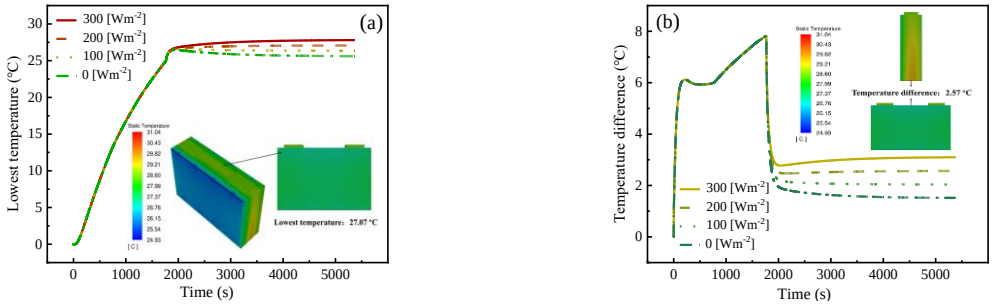

(a) Evolution of minimum temperature **(b) Evolution of temperature difference**

Figure 7. Variation of the minimum battery temperature and temperature difference with time after battery preheating with liquid cooling activated (Case 6 scheme)

Comparing the cases with and without liquid cooling under heating powers of 0-300 [Wm^{-2}] shows that activating the cooling system maintains a higher minimum temperature and reduces the overall temperature difference. Thus, when 25 °C coolant is available after preheating, it is recommended to activate the liquid cooling system during the maintenance phase to better sustain battery temperature and improve temperature uniformity for enhanced thermal management.

4. Conclusion

This study proposes a preheating and thermal maintenance strategy using heating films within a BTMS that combines temperature control and thermal runaway suppression. By comparing different heating configurations and adjusting heating power with the liquid cooling system activated or deactivated, optimal battery temperatures were maintained during the 1 C charging process. Key conclusions are summarized as follows.

(1) Heat flux density significantly affects the temperature difference during battery preheating. The study shows that heating both the minor side and bottom surfaces of the battery improves preheating efficiency, while heating the battery and BTMS together reduces the temperature difference. To balance heating rate and temperature control, it is recommended to use a larger heating area and lower heat flux density during preheating. With a 2000 [Wm^{-2}] heating power applied to both the battery and BTMS,

the battery reaches 25 °C in 1769 seconds, with the temperature difference maintained at 7.82 °C.

(2) A comparison of heating power effects on the minimum battery temperature and temperature difference was made under two conditions: with and without liquid cooling. Results show that without liquid cooling, at least 800 [Wm^{-2}] is needed to keep the minimum battery temperature above 25 °C, but the temperature difference remains large. With liquid cooling activated, the battery temperature stays above 25 °C even without heating power. For more stable temperature control, a 200 [Wm^{-2}] heating power during the thermal maintenance phase is recommended, keeping the minimum battery temperature around 27 °C and the temperature difference at about 2.6 °C.

Acknowledgements

This research is financially supported by the Henan Provincial Department of Science and Technology Research Project (No. 252102241001), the Doctoral Scientific Research Foundation of Zhengzhou University of Light Industry (Grant No. 2021BSJJ043) and the Postdoctoral Fellowship Program of CPSF (Grant No. GZC20250611).

Nomenclature

BTMS	Battery thermal management system	Q_h	natural convection heat transfer rate, [$Wm^{-2}K^{-1}$]
$C_{p,b}$	the specific heat capacity of the battery, [$Jkg^{-1}K^{-1}$]	S	surface area, [m^2]
$C_{p,pcm}$	the specific heat of the PCM, [$Jkg^{-1}K^{-1}$]	T_w	the temperature of the coolant, [K]
$C_{p,w}$	the specific heat of the coolant, [$Jkg^{-1}K^{-1}$]	T_{air}	the ambient temperature, [K]
C_i	inertia coefficient, [m^{-1}]	T_{wall}	the wall temperature, [K]
f_1	the liquid phase volume fraction	β	thermal expansion coefficient, [K^{-1}]
h_{PCM}	specific enthalpy of phase change material, [$kJkg^{-1}$]	λ_x, λ_y, λ_z	the heat conductivity of the battery in the x, y, and z directions, [$Wm^{-1}K^{-1}$]
h_s	specific enthalpy of porous metal foam, [$kJkg^{-1}$]	λ_w	thermal conductivity of the coolant, [$Wm^{-1}K^{-1}$]
K	permeability	μ_w	the dynamic viscosity of the coolant, [kgm^{-3}]
LCT	Liquid cooling tube	ρ_b	density of the battery, [kgm^{-3}]
m_b	the mass of the battery, [kg]	ρ_{PCM}	density of the PCM, [kgm^{-3}]
q_a	the volumetric heat generation rate of the battery during charging and discharging, [Wm^{-3}]	ρ_W	density of the coolant, [kgm^{-3}]
Q	the heat generated by the battery, [W]	τ	time, [s]

References

[1] Wu, S. J., *et al.,* The State of the Art on Preheating Lithium-Ion Batteries in Cold Weather, *Journal of Energy Storage*, *27* (2020), 101059, https://doi.org/10.1016/j.est.2019.101059

[2] Lei, Z. G., Zhai, J. W., Comparison Between Detailed Model and Simplified Models of a Li-Ion Battery Heated at Low Temperatures, *Thermal Science*, *27*(2023), pp.1265-1275, http://doi.org/10.2298/TSCI220128175L

[3] Liu, Y. J., *et al.,* Temperature-Aware Charging Strategy for Lithium-Ion Batteries with Adaptive Current Sequences in Cold Environments, *Applied Energy*, *352* (2023), 121945, https://doi.org/10.1016/j.apenergy.2023.121945

[4] Cui, W., *et al.,* Modeling and Research on High-Frequency AC Heating System for Lithium-Ion Battery Based on Bidirectional Buck-Boost Topology, *Applied Thermal Engineering*, *254* (2024), 123890, http://doi.org/10.1016/j.applthermaleng.2024.123890

[5] Ghassemi, A., *et al.,* Impact of High-Amplitude Alternating Current on LiFePO4 Battery Life Performance: Investigation of AC-Preheating and Microcycling Effects, *Applied Energy*, *314* (2022), 118940, https://doi.org/10.1016/j.apenergy.2022.118940

[6] Tang, A. H., *et al.,* Orthogonal Design Based Pulse Preheating Strategy for Cold Lithium-Ion Batteries, *Applied Energy*, *355* (2024), 122277, https://doi.org/10.1016/j.apenergy.2023.122277

[7] Zhuang, Z. X., *et al.,* Distribution of Relaxation Times-Based Analysis of Aging Mechanisms and Prediction of Heating Domain for Alternating Current Pulse Self-Heating Lithium-Ion Batteries, *Journal of Power Sources*, *623* (2024), 235442, https://doi.org/10.1016/j.jpowsour.2024.235442

[8] Wang, Y. J., *et al.,* Low Temperature Preheating Techniques for Lithium-Ion Batteries: Recent Advances and Future Challenges, *Applied Energy*, *313* (2022), 118832, https://doi.org/10.1016/j.apenergy.2022.118832

[9] Xu, X. B., *et al.,* Low Cost Energy-Efficient Preheating of Battery Module Integrated with Air Cooling Based on a Heat Spreader Plate, *Applied Thermal Engineering*, *232* (2023), 121024, https://doi.org/10.1016/j.applthermaleng.2023.121024

[10] Bao, J. K., *et al.,* Experimental Study on Liquid Immersion Preheating of Lithium-Ion Batteries Under Low Temperature Environment, *Case Studies in Thermal Engineering*, *60* (2024), 104759, http://doi.org/10.1016/j.csite.2024.104759

[11] An, Z. G., *et al.,* Cooling and Preheating Performance of Dual-Active Lithium-Ion Battery Thermal Management System Under Harsh Conditions, *Applied Thermal Engineering*, *242* (2024), 122421, https://doi.org/10.1016/j.applthermaleng.2024.122421

[12] Zhong, Q. X., *et al.,* A Novel Preheating Systems for Columnar Lithium Batteries for Below Zero Degrees Celsius Environment Based on Topology Optimization, *International Communications in Heat and Mass Transfer*, *158* (2024), 107789, https://doi.org/10.1016/j.icheatmasstransfer.2024.107789

[13] Ren, R. Y., *et al.,* Experimental Study on Preheating Thermal Management System for Lithium-Ion Battery Based on U-Shaped Micro Heat Pipe Array, *Energy*, *253* (2022), 124178, https://doi.org/10.1016/j.energy.2022.124178

[14] Liang, L., *et al.,* Experimental Investigation of Preheating Performance of Lithium-Ion Battery Modules in Electric Vehicles Enhanced by Bending Flat Micro Heat Pipe Array, *Applied Energy*, *337* (2023), 120896, https://doi.org/10.1016/j.apenergy.2023.120896

[15] Chen, Z. G., *et al.,* Numerical Investigation and Optimization of Battery Thermal Management Systems Based on Phase Change Material Coupled with Heating Plates in Low Temperature Environment, *Journal of Energy Storage*, *101* (2024), 113875, https://doi.org/10.1016/j.est.2024.113875

[16] An, Z. G., *et al.,* Cooling and Preheating Behavior of Compact Power Lithium-Ion Battery Thermal Management System, *Applied Thermal Engineering*, *226* (2023), 120238,

https://doi.org/10.1016/j.applthermaleng.2023.120238

[17] Zhang, J. Y., *et al.,* Experimental Study on the Low-Temperature Preheating Performance of Positive-Temperature-Coefficient Heating Film in the Prismatic Power Battery Module, *Applied Thermal Engineering*, *258* (2025), 124798, https://doi.org/10.1016/j.applthermaleng.2024.124798

[18] E, J. Q., *et al.,* Effects of Heating Film and Phase Change Material on Preheating Performance of the Lithium-Ion Battery Pack with Large Capacity Under Low Temperature Environment, *Energy*, *284* (2023), 129280, https://doi.org/10.1016/j.energy.2023.129280

[19] Liu, Y., *et al.,* Role of Porous Metal Foam on Temperature Control and Thermal Runaway Propagation of Integrated Battery Thermal Management Systems, *Applied Thermal Engineering*, *267* (2025), 125712, https://doi.org/10.1016/j.applthermaleng.2025.125712

[20] Zhang, W. C., *et al.,* Influence of Phase Change Material Dosage on the Heat Dissipation Performance of the Battery Thermal Management System, *Journal of Energy Storage*, *41* (2021), 102849, https://doi.org/10.1016/j.est.2021.102849

[21] Xu, X. B., *et al.,* Performance Analysis of Thermal Management Systems for Prismatic Battery Module with Modularized Liquid-Cooling Plate and PCM-Negative Poisson's Ratio Structural Laminboard, *Energy*, *286* (2024), 129620, https://doi.org/10.1016/j.energy.2023.129620

[22] Zhou, H. B., *et al.,* Thermal Performance of A Hybrid Thermal Management System that Couples PCM/Copper Foam Composite with Air-Jet and Liquid Cooling, *Journal of Energy Storage*, *74* (2023), 109408, https://doi.org/10.1016/j.est.2023.109408

[23] Malik, M., *et al.,* Review on Use of Phase Change Materials in Battery Thermal Management for Electric and Hybrid Electric Vehicles, *International Journal of Energy Research*, *40* (2016), 8, pp. 1011-1031, https://doi.org/10.1002/er.3496

[24] Zhang, W. C., *et al.,* Avoiding Thermal Runaway Propagation of Lithium-Ion Battery Modules by Using Hybrid Phase Change Material and Liquid Cooling, *Applied Thermal Engineering*, *184* (2021), 116380, https://doi.org/10.1016/j.applthermaleng.2020.116380

[25] Li, W. H., *et al.,* Design and Optimization of an Integrated Liquid Cooling Thermal Management System with a Diamond-Type Channel, *Thermal Science and Engineering Progres*s, *47* (2024), 102325, https://doi.org/10.1016/j.tsep.2023.102325

[26] Li, Y., *et al.,* Battery Thermal Management Model and Structure Optimization of Porous Composite Phase Change Material, *Chinese Science Bulletin*, *65* (2019), 2, pp. 213-221, https://doi.org/10.1360/tb-2019-0285

[27] Yang, X. H., *et al.,* Role of Porous Metal Foam on the Heat Transfer Enhancement for a Thermal Energy Storage Tube, *Applied Energy*, *239* (2019), pp.142-156, https://doi.org/10.1016/j.apenergy.2019.01.075

[28] Zhang, W. C., *et al.,* Non-Uniform Phase Change Material Strategy for Directional Mitigation of Battery Thermal Runaway Propagation, *Renewable Energy*, *200* (2022), pp.1338-1351, https://doi.org/10.1016/j.renene.2022.10.070

RECEIVED DATE: 26.01.2026.
DATE OF CORRECTED PAPER: 16.3.2026.
DATE OF ACCEPTED PAPER: 13.5.2026,